SAHLGRENSKA ACADEMY

Effects of reconstruction parameters on the image quality and quantification of PET images from PET/MRI and PET/CT systems

M.Sc. Thesis

Amena Ali Hussain

Essay/Thesis:	30 hp
Program and/or course:	Medical physics
Level:	Second Cycle
Semester/year:	Autumn 2021
Supervisor:	Esmaeil Mehrara, Eva Forssell-Aronsson, Tobias Rosholm
Examiner:	Magnus Båth

Abstract

Essay/Thesis:	30 hp
Program and/or course:	Medical physics
Level:	Second Cycle
Semester/year:	Autumn 2021
Supervisor:	Esmaeil Mehrara, Eva Forssell-Aronsson, Tobias Rosholm
Examiner:	Magnus Båth
Keyword:	PET/CT, PET/MRI, OSEM, BPL, NEMA IQ

Aim: To study how reconstruction parameters affect the positron emission tomography (PET) image quality and quantitative results for the different lesion to background radioactivity ratios in three different PET systems.

Introduction: Multimodality imaging that combines magnetic resonance imaging (MRI) or computed tomography (CT) with a PET system can produce medical images containing both functional and anatomical information. The most used PET reconstruction algorithm in clinical systems is Ordered Subset Expectation Maximization (OSEM) with time-of-flight (TOF) and point spread function (PSF). In the OSEM algorithm, the image noise increases as the number of iterations increases. Thus, the reconstruction needs to be stopped before a complete convergence can be achieved. The Bayesian Penalized Likelihood (BPL) reconstruction algorithm (''Q-clear'') has been newly introduced to reconstruct PET images, which applies a penalty method for image noise suppression so that the iterations can continue to full convergence. The image quality and noise suppression in the BPL can be controlled by the noise penalty factor (β). BPL algorithms are shown to improve signal-to-noise in PET images.

Method: A NEMA IQ phantom was scanned on GE Signa PET/MRI, GE Discovery MI PET/CT, and Siemens Biograph mCT PET/CT system with 2:1, 4:1, and 10:1 sphere-to-background radioactivity concentration ratios of the 2-[^{18}F]FDG solution. Acquired list-mode data were used to reconstruct PET images with either OSEM or Q-clear algorithms, with and without TOF. The number of iterations and β-values were varied, while the matrix size, number of subsets, and filter size were kept constants for all reconstructions. After reconstruction, the images were evaluated and compared using the NEMA analysis tools available for each system, using automatic localisation of the region-of-interests (ROI). Contrast recovery (CR) and background variability (BV) values were determined for each ROI in all reconstructed PET images to assess the image quality and quantification accuracy.

Result: Results showed that CR increased with increased sphere size from 10 mm to 22 mm in diameter and activity concentration ratios (sphere to background) from 2:1 to 10:1. CR and BV decreased gradually in reconstructed images with increased β-values for the smallest sphere, i.e., 10 mm in diameter. Increased number of iterations in OSEM algorithm showed to increase BV with low significant variation of CR. The comparison between reconstruction algorithms showed higher CR values and lower BV values with Q-clear than with OSEM. Reconstructed PET images with TOF showed higher CR and lower BV than reconstructions without TOF for both algorithms. The optimal reconstruction parameters were for GE-Signa and Discovery MI systems a β-value between 150 and 350 for TOF Q-clear, and three iterations, 16 subsets, 5 mm FWHM Gaussian filter for TOF OSEM. For the Biograph mCT system, the optimal reconstruction parameters were two iterations, 21 subsets, and 5 mm FWHM Gaussian filter for OSEM algorithm with TOF.

Conclusion: PET images acquired on GE Discovery MI PET/CT and reconstructed with the Q-clear algorithm provided the best image quality and quantitative accuracy for the smallest sphere.

List of abbreviations

AC	Attenuation correction
APD	Avalanche photodiode
BV	Background variability
BPL	Bayesian penalized likelihood
CR	Contrast recovery
CT	Computed Tomography
2-[^{18}F]FDG	2-deoxy-2-[fluorine-18] fluor-D-glucose
GE	General Electric
IQ	Image quality
LBS	Lutetium based scintillators
LOR	Line-of-response
LSO	Lutetium oxyorthosilicate
LYSO	Lutetium-yttrium oxyorthosilicate
MRI	Magnetic resonance imaging
NEMA	National Electrical Manufacturers Association
OSEM	Ordered Subset Expectation Maximization
PMT	Photomultiplier tubes
PET	Positron emission tomography
PSF	Point spread function
ROI	Region of interest
SiPM	Silicon photomultiplier
SBR	Sphere-to-background activity concentration ratio
SUV	Standardized uptake value
TOF	Time-of-flight

Table of content

1. Introduction

The concept of medical imaging led to a dramatic change in healthcare. It began in 1895 when the physicist Wilhelm Conrad Röntgen discovered an x-ray which made it possible to view the inside of the body (1). Nevertheless, the development of medical diagnostic technology did not stop right there, and in the second half of the 20th century, a revolution started with the continued development of important diagnostic imaging modalities and techniques (2).

Positron emission tomography (PET) is one of those modalities that have continuously developed over the past six decades (3), and today is one of the most important cancer imaging tools in nuclear medicine. PET technology has advanced immensely, which has led to advanced techniques and integrated with other modalities, computed tomography (CT) or magnetic resonance imaging (MRI). The purpose of the combination is to produce medical images of different functional and anatomical information simultaneously. This information makes it possible to provide an accurate diagnosis, staging, and restaging, especially for the therapeutic management of cancer patients.

A PET examination uses a radiopharmaceutical glucose analogue, and the glucose analogue 2-deoxy-2-[fluorine-18] fluor-D-glucose (2-[^{18}F]FDG) is the most commonly used PET tracer. This tracer provides valuable functional information such as the glucose uptake and glycolysis rate and illustrates metabolic abnormalities before morphological changes can be visualized. The principle is that when 2-[^{18}F]FDG is injected into a vein, it accumulates more in malignant cells due to increased glucose uptake than normal cells (4), and results in a higher signal in the acquired PET images (5). Semi-quantitative analysis with standardized uptake value (SUV) can be used to improve the accuracy and consistency of 2-[^{18}F]FDG in PET images (6). SUV is commonly used as a parameter to assess tumor response to the treatment.

1.1 PET

Positron emission tomography (PET) is a functional imaging technique that enables a non-invasive quantitative measurement of biological processes in vivo. Tomographic imaging with PET requires injecting the patient with a radioactive substance that emits positrons. The emitted positron will then interact with its antiparticle, electron, and an annihilation pair of photons will be emitted with identical energy of 0.511 MeV.

The photons will be emitted with approximately 180 degrees angle to each other and can be detected with the surrounding PET-detectors (7). A line of response (LOR) is formed by detecting the path of a pair of coincident photons from the tracer until they hit the opposing detectors, as shown in figure 1. The limitation of LOR is that it cannot decide the exact position of the annihilation along the line of LOR. The Time-of-flight (TOF) method makes it possible to estimate the position by considering the time difference between the detection of the two annihilation photons (8).

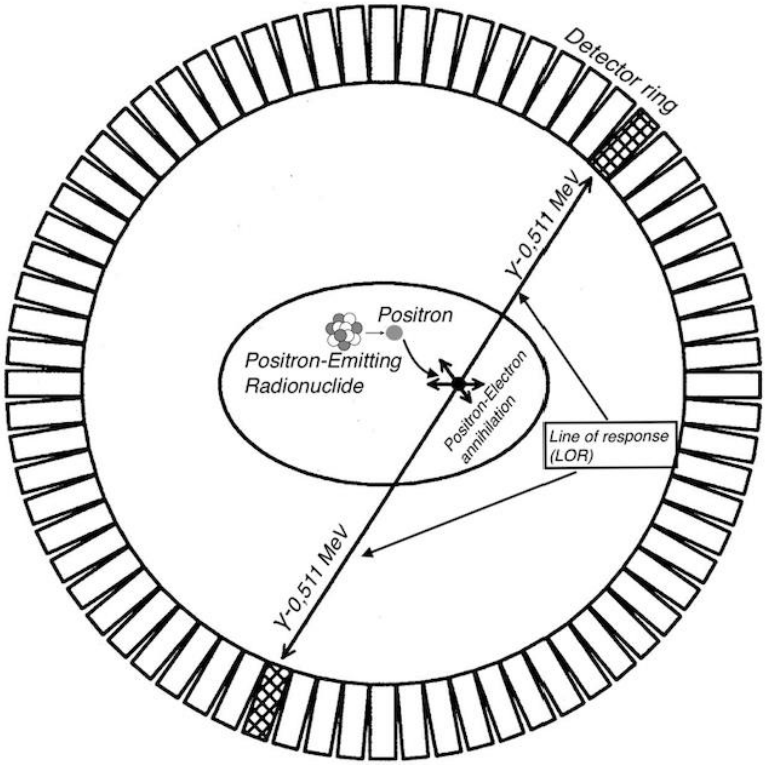

Figure 1: The positron-electron annihilation at PET examination. A pair of annihilation photons are emitted back-to-back at 180 degrees in the opposite direction and toward detectors. The figure is redrawn from reference (9).

Lutetium based scintillators (LBS) such as lutetium oxyorthosilicate (LSO) or lutetium yttrium oxyorthosilicate (LYSO) scintillators crystals are widely used detector materials in PET systems. These crystal types have favorable properties for the PET system due to its high effective atomic number (Z) and density, which provide fast timing, high energy solution, and high stopping power, due to its convenient physical properties for absorbing gamma radiation and converting it to light. Then, the photomultiplier tubes (PMT) convert the light to signal. This good timing resolution of LBS makes it possible to apply the time-of-flight (TOF) method for PET scanning to achieve a better spatial resolution, sensitivity, and even more to reduce the statistical noise (10).

In order to present the collected raw data from the PET scan, it is necessary to organize the data in a matrix in planar imaging so that a 2D matrix is created, which is called a sinogram. LOR that passes through the region of interest (ROI) will correspond to a particular pixel in the sinogram depending on its orientation angle and the distance from the center of the gantry (11). Every sinogram corresponds to a slice that can be reconstructed. However, the collected data in the sinogram is not perfect until it gets corrected for some effects. The effects that have to be considered are photon attenuation, the variation of detection efficiency, and the accidental (or random) coincidences and scattered coincidences recorded along with the true coincidences (12).

Emitted photons will attenuate differently depending on which part of the body they pass through. Dense materials absorb or scatter the photons more than sparser materials, and impairs the image quality and lead to inaccurate quantification of radionuclide trace uptake. Attenuation correction (AC) needs to be used to correct the impaired effect. The AC for sinograms is obtained by performing a blank scan and a transmission scan using an external radiation source that transmits photons through the body to the detector. The ratio between the blank sinogram and the transmission sinogram represents the AC factor. When the sinogram is corrected for attenuation, it is ready to be reconstructed (13, 14).

The PET scan is mainly used to study functional parameters, such as metabolism and perfusion, but there is usually a lack of anatomical information. For clinical examinations, information is important to determine the anatomical location of, e.g. the tumor in the body. Therefore, PET systems integrated with CT or MRI have been developed to compensate for this.

1.2 PET/CT

Integrated PET/CT scanners are widely used (15). An advantage of the PET/CT scan is that CT can generate fast transmission images with high statistical quality that can be used for attenuation correction (AC) and scatter correction for PET emission data. CT-based AC reduces at least 40% of whole-body imaging time and creates a noiseless AC factor compared to standard PET transmission AC factors (15).

To use CT-based AC for PET images, the pixel intensities in CT images, expressed in Hounsfield units (HU), need to be transformed into a linear attenuation coefficient (μ) for the PET energy level of 511 keV. This is done by plotting the linear attenuation coefficient at 511 keV against the CT values in Hounsfield units (HU) for different x-ray energies in the range of 40-140 keV. A different scaling factor is used for soft tissues, air, water, and bone. Bilinear fit to these points is commonly used to scale the CT numbers for attenuation correction of the PET data (16, 17), as illustrated in figure 2.

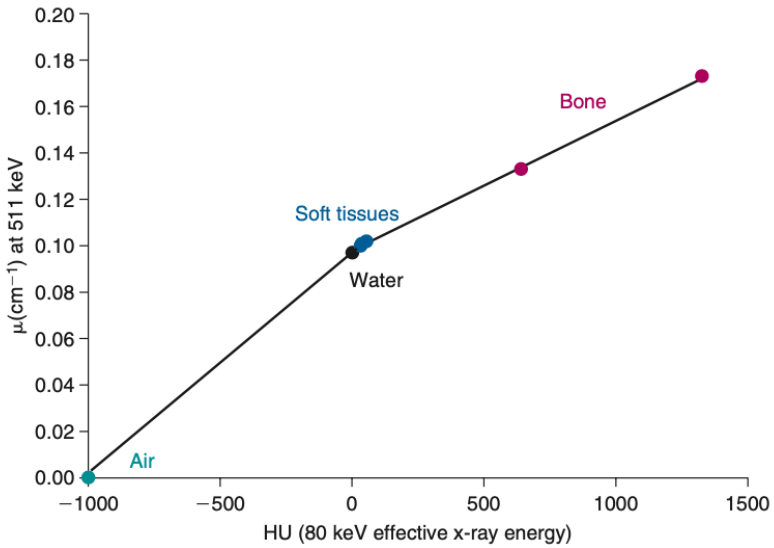

Figure 2: A 511 keV linear attenuation coefficient (μ) of water, soft tissues, bone, and air, as a function of CT number in Hounsfield units for 80 effective keV x-ray. A bilinear fit to these points translates CT attenuation numbers to PET 511-keV attenuation data. Data obtained from reference (17).

One of the larger concerns in PET/CT is the high radiation dose the patient will be exposed to. The patient receives ionising radiation both from the radiopharmaceutical and CT examination, which is important for anatomical correlation and attenuation correction.

A recent study reported the estimated effective doses from whole-body ^{18}F-FDG PET/CT scan. The results showed an effective dose between 1.6 and 9.9 mSv (18), which was found to be lower than the International Commission on Radiological Protection (ICRP) values (19). The patient doses were also lower than previous studies reporting to be 14 in males (20) and 17.2 mSv in females. Based on the result, the study concluded that whole-body imaging using the ^{18}F-FDG PET/CT can significantly be reduced the patient extremity dose while maintaining the image quality.

1.3 PET/MRI

Multimodality imaging with PET/MRI is a recently developed combination that has become a large active research area. Combining PET with MRI, which provides structural imaging and better soft tissue contrast than CT, is especially beneficial in areas with nearby soft tissue types,

such as the brain, abdomen, and pelvis. MRI imaging also provides several physiological and functional imaging contrast mechanisms, e.g., MR spectroscopy, diffusion imaging, and functional MRI (21).

The building of PET/MRI systems requires overcoming certain limitations and challenges when combining multiple systems. MRI systems create high magnetic fields and radio frequency waves (RF). Conventional PET detectors use PMT that can interfere with the magnetic field homogeneity or introduce noise by the MRI-scan. This technical challenge can be solved by using a PET detector that is not affected by the magnetic field from MRI systems (22).

Developed solid-state detectors in PET are used, such as avalanche photodiodes (APDs) and silicon photomultipliers (SiPMs). Both these photodetectors have similar geometry and performance. On the other hand, SiPMs provide improved time resolution, allowing TOF to improve the signal-to-noise ratio (SNR). Siemens Healthcare uses APDs in the Biograph mMRI PET/MRI system, and SiPMs were recently introduced by General Electric (GE) Healthcare and used in GE SIGNA PET/MRI systems. Those detectors make it possible to integrate the PET-detector ring inside the bore of an MRI scanner, leading to a fully integrated system that enables simultaneous PET- and MRI-imaging (22, 23).

The second particular challenge with PET/MRI systems is when MRI images are used to create AC for PET emission data. MRI images contain signals related to proton density and longitudinal (T1) and transverse (T2) magnetization relaxation properties of the examined tissue and do not consider the attenuation of ionizing radiation in tissue (24). Therefore, MRI-based AC can lead to incorrect quantitative and semi-quantitative estimation of PET data. Several MRI-based AC methods have been proposed and are divided into three types.

- Segmentation method, including Dixon T1-weighted imaging (T1W) using ultrashort echo sequence. These methods perform segmentation of different tissues so a well-defined linear attenuation coefficient can be estimated for each tissue.

- Atlas-based (template) methods use a co-registered database or atlas of CT and MRI images from a group of patients.
- PET emission-based data methods, where the AC maps are generated from TOF PET data.

Combining these methods with machine learning techniques makes AC possible for a certain part of the body with PET/MRI systems (25).

However, when imaging a phantom such as the National Electrical Manufacturers Association (NEMA) phantom, it is preferred to use the CT-based template μ-map for the filled NEMA image quality (IQ) phantom. The purpose is to avoid artifacts and signal inhomogeneities that can occur, due to RF-wave phenomena and T1 effects, in MRI-based AC for NEMA phantom during PET/MRI imaging (26).

1.4 Reconstruction algorithm and parameters

Advanced imaging methods that combine MRI or CT with 2-[^{18}F]FDG PET can improve accurate diagnosis and staging of tumors. However, there are limitations in detecting small lesions due to relatively low SNR and limited spatial resolution. Therefore, there have been several technical developments in PET technology in the last decade. The inclusion of new hardware features such as TOF acquisition and advanced image reconstruction methods using iterative reconstruction algorithms have improved PET images (26, 27).

The reconstruction algorithm of PET raw data is based on iterative methods, and the most common algorithm in clinic systems is Ordered Subset Expectation Maximization (OSEM). OSEM is an accelerated reconstruction process that allows the modelling of various system factors in the reconstruction process, such as point spread function (PSF) and TOF (27).
PSF correction in PET images improves spatial resolution, minimizes partial volume effects, and increases SNR in PET images. Nonetheless, PSF-based reconstruction can alter quantitative accuracy because it can cause edge artifacts (known as Gibb's artifacts). It occurs as overshoot

and ringing around the sharp changes of intensity. OSEM reconstruction with PSF and TOF has shown better lesion detectability and better quantification with SUV of the small lesion (28).

The largest disadvantage of OSEM is a trade-off between the number of subsets, iterations, and image quality. OSEM divides the projections into subsets which are analyzed sequentially during each iteration. When the number of subsets increases, noise and artifacts may increase. The problem appears because the subset contains a small amount of tomographic and statistical information. An increased number of iterations also leads to increased background noise, reducing accuracy and image quality. Thus, the OSEM algorithm is often stopped before complete convergence will be achieved (29, 30).

Bayesian penalized likelihood (BPL), so-called ''Q-clear'', is the newly introduced algorithm by GE-Healthcare that includes PSF modelling and relatively different penalties. The penalty is a function of the difference in values between adjacent voxels and their sum. Many parameters control this penalty function, but only the noise penalty factor (β) can be varied and controls noise suppression. Unlike OSEM, an increased number of iterations in a BPL algorithm does not increase noise, and an effective convergence can be achieved in the image. BPL has also been shown to significantly improve signal-to-noise and SUV in clinical scans compared to OSEM, especially in small lesions (31). High β-values result in stronger noise suppression, but on the other hand, it can affect other things like edge detection and volume determination. The optimal β-values in clinical praxis are necessary to estimate, with a balance between the calculated statistics and the resulting image quality (30).

PET-image quality and quantification depend on the choice of reconstruction algorithms and PET systems. The parameters SNR and contrast-to-noise ratio (CNR) may be used to determine image quality and SUV parameters to assess image quantification. These parameters make it possible to compare results and even lead to a harmonized interpretation of images regardless of the camera used for imaging (32).

1.5 NEMA IQ phantom

In diagnostic medical imaging, it is required to control and evaluate the performance of imaging modalities regularly to ensure the proper functionality and optimal image quality (33). The NEMA IQ phantom has been defined as a standard for assessing the performance of PET systems. Such measurements are also applied for hybrid imaging (such as PET/CT and PET/MR) for image quality control of the PET component (34). Image quality control is conducted when a new system is introduced or on a regular basis when monitoring the quality of a specific PET system.

One of the measures of PET image quality is image contrast, which reflects the differences in pixel intensities between different radioactive concentration levels (35). With NEMA IQ phantom, contrast recovery (CR) and background variability (BV) can be analysed. The CR value is the ratio between the measured and true concentrations in an ROI. BV reflects the noise level of the image, and the higher BV, the higher level of image noise. These parameters can be used to investigate the impact of various reconstruction algorithms and parameters in the reconstructed image.

1.6 Aims

The aims of the project were to compare how OSEM and BPL recontraction algorithms affect the resulting image quality and quantitative measures for three PET systems, for different lesion to background 2-[^{18}F]FDG concentration ratios using NEMA IQ phantom.

2. Material and methods

2.1 Phantom preparation

NEMA IQ phantom was used to collect data. The phantom volume is 9.8 liters and contains six fillable spheres with internal diameters of 10, 13, 17, 22, 28 and 37 mm, respectively, and in the present study regarded as tumors. The phantom also includes plastic filled material with a low atomic number to represent the lung (with an average density of 0.3 g/ml) and lung attenuation, centered inside the phantom body and extending axially through the entire phantom.

Figure 3: NEMA IQ phantom with a lung insert and six fillable spheres of knowns internal diameters (35).

The sphere-to-background activity concentration ratios (SBR) were chosen based on data from previous patient PET/CT scans using gallium-68-prostate-specific membrane antigen [^{68}Ga]Ga-PSMA-11 or 2-[^{18}F]FDG. Table 1 shows the concise overview of the T/B activity concentration ratio for different tumors. Based on the data, the phantom was filled with a homogenous solution of 2-[^{18}F]FDG (half-life ($T_{1/2}$)) of 110 minutes to obtain a SBR values of 2:1, 4:1, and 10:1. This resulted in an activity concentration of 10, 20 and 20 kBq/ml in the hot spheres, while the background activity concentrations were 5, 5 and 2 kBq/ml, respectively.

The phantom preparation started by filling the phantom background with 50%, 25%, or 10 % of the total phantom volume with water. A precise measuring volumetric flask was used to scale water volume. An injector system was used to fill the phantom background with 49 MBq (for SBR 2:1 and 4:1) or 20 MBq (for SBR 10:1) at scan time. The solution in the phantom was shaken carefully to obtain homogeneity. Afterwards, 13 ml of 2-[^{18}F]FDG solution was removed from the background of the phantom with a 10 ml volume syringe and a long needle. The solution was later injected into hot spheres, and the remaining solution in the syringe was returned to the phantom background. The two biggest spheres are nonradioactive, called cold spheres, with 28 and 37 mm diameters filled with water, see figure 4. In the end, the background region of the phantom was refilled to full of water.

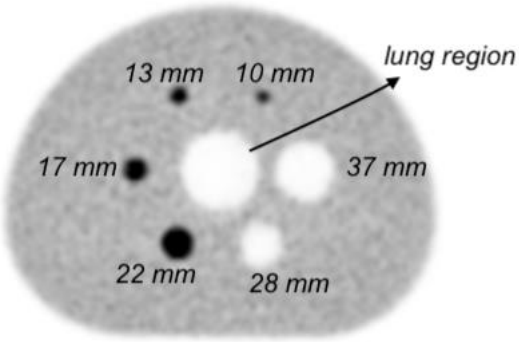

Figure 4: Cross-section of NEMA IQ phantom, illustrating the sphere diameters.

The NEMA phantom was vertically centered on the patient table, and two foams were placed in case of need under the phantom axial end. The landmark aligned in the central plane of spheres is approximately 80 mm from the center of the sphere to the top surface of the phantom.

Table 1: T/B values from 2-[^{18}F]FDG and [^{68}Ga]Ga-PSMA-11 imaging of the patients. The T/B ratio was obtained by dividing tumor signal by surrounding signal from normal tissue or background, and it is performed by drawing ROIs in PET images.

	Radiopharmaceutical	**T/B-R (mean± SD)**	**T/B-R (Median (range))**
Glioma brain tumor (36)	2-[^{18}F]FDG	1.3 ± 0.4	
Positive cardiac lesion (37)	2-[^{18}F]FDG	4.5 ± 1.5	
Primary tumor (38)	[^{68}Ga]Ga-PSMA-11		18.8 (6.7 – 92.0)
Positive Axillary lymph node (39)	2-[^{18}F]FDG	4.5 ± 2.0	
Bone metastases (38)	[^{68}Ga]Ga-PSMA-11		7.8 (1.5–35.0)

2.2 Image acquisition

Data acquisition of the phantom was performed on three different cameras:

- PET/MRI Signa 3T (GE Healthcare, Chicago, Illinois, USA) with 3.0 tesla MR scanner.
- PET/CT Discovery MI (GE Healthcare, Chicago, Illinois, USA).
- PET/CT Biograph mCT (Siemens Healthineers AG, Erlangen, Germany).

Table 2 shows the system specification of PET cameras used in this study (40-42).

Table 2: PET systems specifications for Siemens Biograph mCT, GE Signa, and GE Discovery MI system.

	Biograph mCT	**Signa**	**Discovery MI**
Scintillator material	LSO	LBS	LBS
Scintillator dimensions (mm)	4.0 x 4.0 x 20	3.95 x 5.3 x 25	4.0 x 5.3 x 25
Number of detector rings (Number of detector blocks)	4 (48)	4 (36)	4 (45)
Axial field-of-view (cm)	22.1	20	25
Transaxial field-of-view (cm)	70	70	60
Photomultipliers	PMT	SiPM	SiPM

The GE PET/MRI scan was performed by following the listed steps in the NEMA NU 2-2012 Manual for Signa PET/MRI system. The GE PET/MRI system contains a pre-loaded template of the attenuation map, where is aligned automatically to the scanned phantom data through rigid registration. Therefore, only a three-minute positioning scan was needed, followed by a PET scan under varying acquisition time depending on SBR at scanning and the time from calibration of 2-[^{18}F]FDG to imaging. The scan time was increased concerning physical decay if the imaging acquisition started after the planned time. Table 3 shows PET image acquisition time and 2-[^{18}F]FDG activity concentration for the hot sphere (A_H) and the phantom background (A_B) at time for scanning. All emission data were acquired in list mode to be able to reconstruct the data afterwards.

Data acquisition with GE PET/CT and Siemens PET/CT was similar. The imaging started with an overview of the phantom, a scout scan, which gives a planar image of the transmission of the x-ray. The scout scan was used to define the axial field of the CT and PET examination. CT-scan was performed with the following parameters: 120 kV tube voltage, automatic tube current (under software control), and 0.5-second pitch. The section thickness was 1.5 mm for Siemens

and 2.78 for GE cameras. The CT-scan aims to generate a CT-based μ-map from CT images used for AC of PET data. Immediately after the CT-scan, the PET scan was performed with the acquisition time presented in table 3. All emission data were also acquired in list mode.

Table 3: PET acquisition time for respectively sphere-to-background ratio (SBR) performed at Siemens PET/CT, GE PET/CT, and GE PET/MRI systems. The hot sphere (A_H) and the phantom background (A_B) 2-[^{18}F]FDG activity concentrations are given at image acquisition start.

Camera system	**SBR**	$\mathbf{A_H}\left(\frac{\mathbf{kBq}}{\mathbf{ml}}\right)$	$\mathbf{A_B}\left(\frac{\mathbf{kBq}}{\mathbf{ml}}\right)$	**Acquisition time (min)**
Siemens Biograph mCT	2:1	9.9	4.9	20
	4:1	18	4.7	10
	10:1	11	1.1	30
GE Discovery MI	2:1	4.7	2.4	40
	4:1	15	3.9	15
	10:1	18	1.8	25
GE Signa	2:1	7.2	3.6	23
	4:1	23	5.7	10
	10:1	7.3	0.73	60

2.3 PET image reconstruction

The standard PET reconstruction algorithms used at our centre, Sahlgrenska University Hospital, are:

- TOF OSEM with three iterations, 16 subsets and a 5 mm FWHM Gaussian filter for GE PET/CT.
- Q-clear with β-value 550 for GE PET/CT.
- TOF OSEM with two iterations, 21 subsets and a 5 mm FWHM Gaussian filter for Siemens PET/CT.

For GE PET/MRI there is no standard protocol for lung reconstruction yet, since it was recently installed at Sahlgrenska University Hospital.

PET images were reconstructed using two algorithms: OSEM (SharpIR) and BPL (Q-clear) with and without TOF (43). Images were reconstructed with one parameter varied at a time, while other parameters were kept constant. In this study, the number of iterations (i) and β-values were varied, as illustrated in table 4. The matrix size was 256x256, and the filter size was set on a full-width-at-half-maximum (FWHM) of 5 mm for all reconstructions. The filter cutoff function operates as a post-filter without TOF and a Gaussian filter with TOF (43). All GE cameras had almost the same reconstruction parameters. It was only possible to vary the number of iterations for OSEM +TOF reconstruction at Siemens, while the number of subsets (s) was constant, 21.

Table 4: Image reconstruction parameters. The PET images were reconstructed with OSEM and Q-clear reconstruction algorithm with and without TOF. The reconstruction parameters varied for all investigated images. s = number of subsets, i = number of iterations.

Camera		**Iterations:Subsets**	**β-value**
GE Discovery MI and GE Signa	-TOF	3i:16s,4i:16s, 6i:16s, 8i:16s, 10i:16s	100, 150, 350, 550, 750, 1000
	+TOF	3i:16s,4i:16s, 6i:16s, 8i:16s, 10i:16s	100, 150, 350, 550, 750, 1000
Siemens Biographs mCT	-TOF	4i:12s, 6i:12s, 8i:12s, 12i:12s	
	+TOF	2i:21s, 3i:21s, 4i:21s, 6i:21s, 8i:21s	

2.4 Data analysis

According to the NEMA standard protocol, PET image quality can be obtained using contrast recovery (CR) and background variability (BV). Various regions-of-interest (ROIs) in the transverses images was evaluated to calculate these parameters, using the NEMA analysis tool

in each system. The analyses for GE PET/CT and GE PET/MR images were performed on SPARC standalone PET reconstruction server (GE Healthcare, Chicago, Illinois, USA) and on Syngo.via (Siemens Healthineers AG, Erlangen, Germany) for Siemens PET/CT images. Figure 5 shows an example of the user interface of the image quality tool where the calculation starts after entering the SBR value.

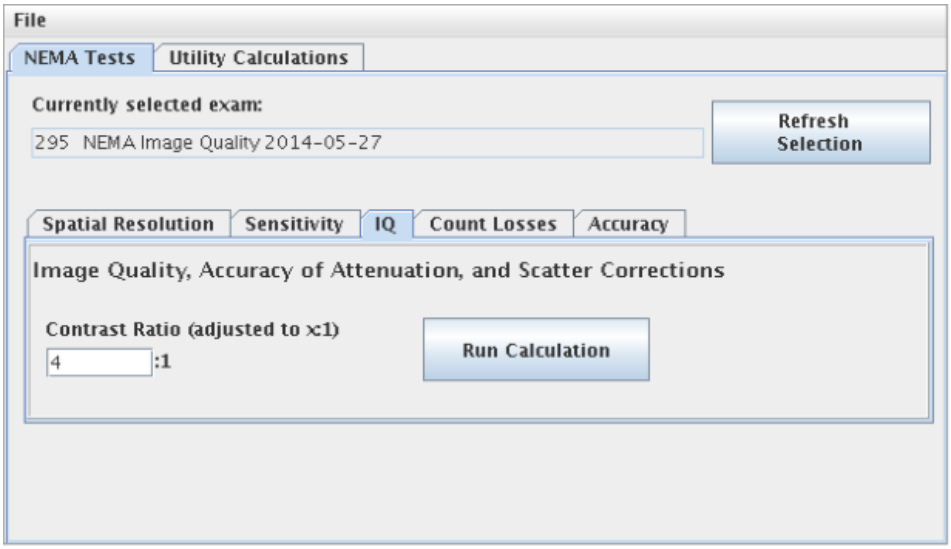

Figure 5: Data field display for PET analysis tool.

The analysing tools automatically positioned the ROI over each of the hot spheres (10, 13, 17, and 22 mm), cold spheres (28 and 37 mm), and in the background area of the reconstructed PET images (figure 6).

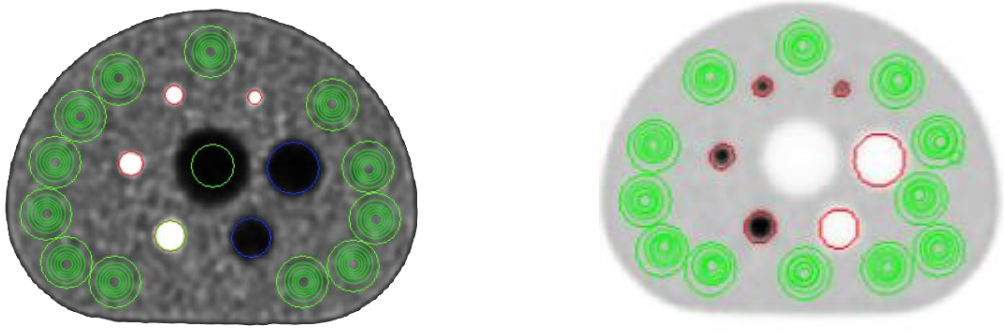

Figure 6: ROI delineation in Syngo.via workstation for Biograph mCT (left) and SPARC workstation for Discovery MI and Signa cameras (right).

CR and BV were determined based on the number of counts and activity in each sphere of interest. The contrast recovery for each hot sphere j was determined by equation 1.

$$CR_{H,j} = \frac{\frac{C_{H,j}}{C_{B,j}} - 1}{\frac{a_H}{a_B} - 1} \times 100\ \% \qquad \text{Equation 1}$$

$C_{H,j}$ is the average number of counts in the ROI in the transverse image slice containing the center of a hot sphere j. $C_{B,j}$ is the average of the number of counts in the twelve background ROIs. The diameter of the background ROI is the same size as sphere j, as illustrated in figure 6. a_H / a_B is the actual activity concentration ratio in the hot-sphere and background volume.

The image noise level for sphere j was measured through the background variability (BV), determined using equation 2. SD_j is the standard deviation of the number of counts in the background ROI for sphere j.

$$BV_j = \frac{SD_j}{C_{B,j}} \times 100\ \% \qquad \text{Equation 2}$$

Excel was used to analyse the statistically significant differences between acquired data from different reconstructions for a specific ROI of the sphere in the phantom. A two-way analysis of variance (ANOVA) was used with a confidence interval of 95% and a significance level of 0.05.

3. Results

3.1 Contrast recovery analysis

3.1.2 Q-clear reconstruction

Figure 7 shows the CR of the NEMA phantom hot spheres for PET images obtained with Discovery MI and the Signa systems with varying SBR and β-values. All plots show a similar trend; CR for hot spheres increases with reduced β-value and increased sphere size. The results in figure 7 showed an increase in CR by more than 100 %, with the increase of SBR from 2:1 to 10:1, in the smallest sphere. SBR 2:1 result from Discovery MI are missing CR for the 22 mm sphere since the NEMA analyses tool failed to delineate the sphere properly because data acquisition was performed one and a half hours after the planned time and image acquisition time could not be prolonged. The ROIs could not be placed manually. The steadiest CR decrease with increased β-value occur for the 10 mm and 13 mm spheres compared with the 22 mm sphere.

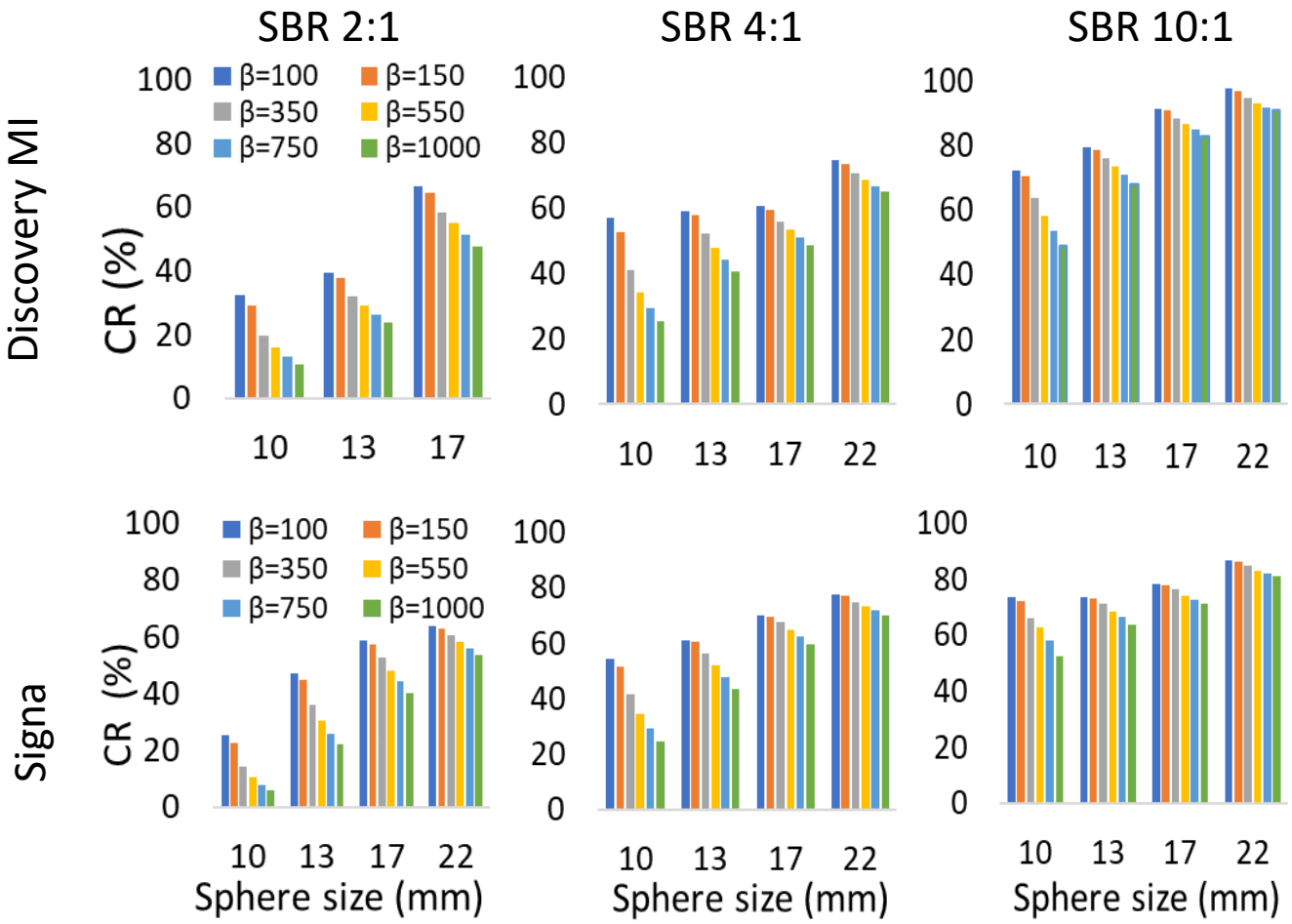

Figure 7: CR versus sphere size for Discovery MI and Signa systems with varying β and SBR values. All reconstructions used a constant matrix size of 256x256 and 5 mm FWHM Gaussian filter.

3.1.2 OSEM reconstruction

The result of the reconstruction using the OSEM algorithm for PET images performed on all three cameras with different SBR values is illustrated in figure 8. The figure shows a trend of increased CR with increased sphere size and SBR for all PET systems. For SBR 10:1, the obtained PET images from both Discovery MI and Biograph mCT did not show a large CR variation in CR between different iterations. However, for the Signa system the largest variation for SBR 10:1 was shown, and CR declined by around 25 % from iteration three to iteration ten due to a large reduction of CR for iteration 10. This large variation for the 10 mm sphere is observed in all plots (figure 8) and was highest for the Biograph mCT SBR 2:1 with an increase of 52 % from

two to eight iterations. No substantial variation of CR was observed for the Discovery MI SBR 10:1 with a varied number of iterations.

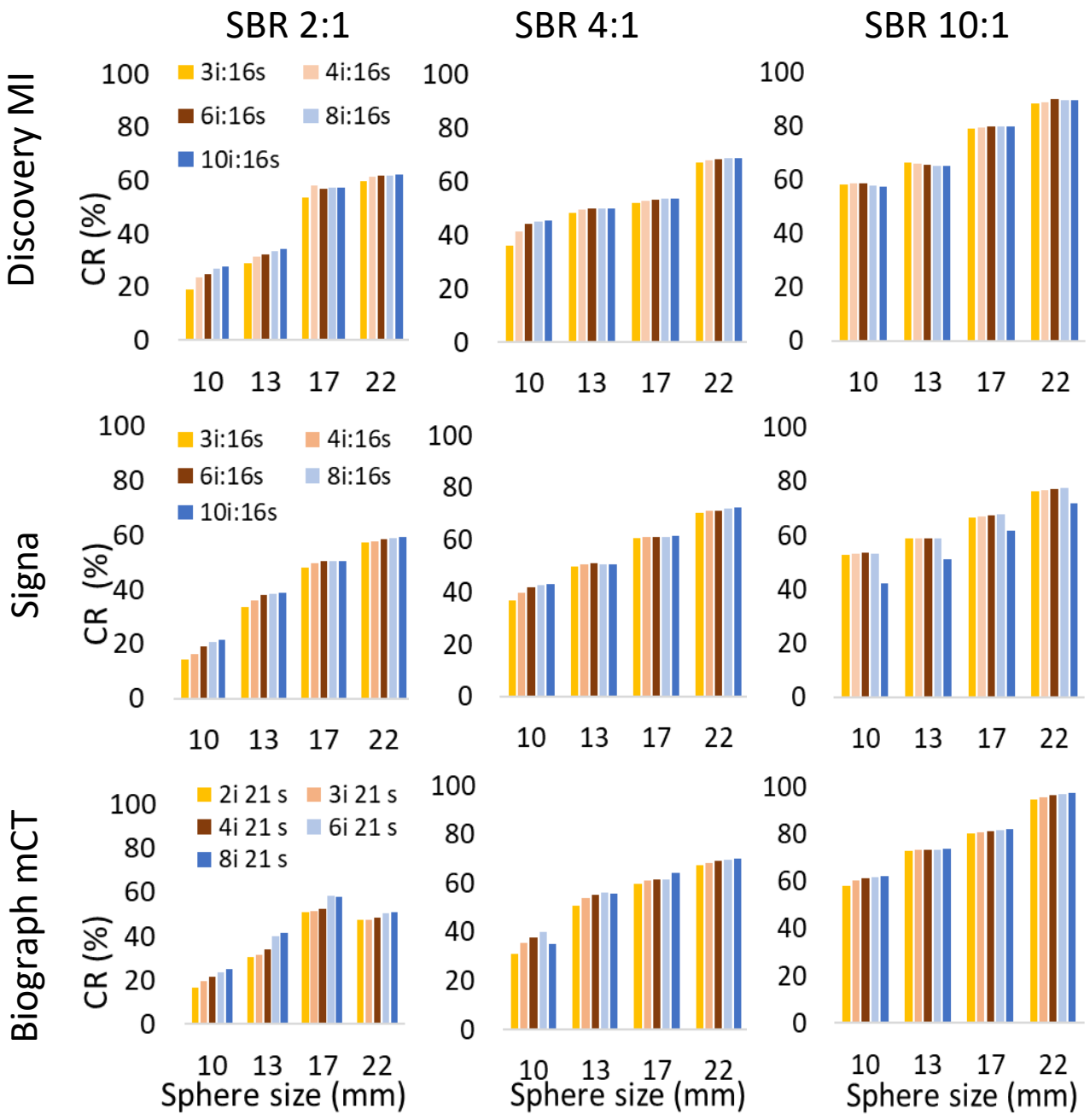

Figure 8: CR for varying number of iterations (2-10) in OSEM algorithm as a function of sphere size for different PET systems and SBR. All reconstructions were made with a constant matrix size of 256x256 and a 5 mm FWHM Gaussian filter.

3.2 Contrast recovery versus background variability

The effects of changing the reconstruction parameters in OSEM and Q-clear reconstruction algorithm were investigated to evaluate how this would impact estimations quantifications of radioactivity concentration in spheres and image noise. In this study, the 10 mm sphere was chosen for further analysis due to the highest variation observed between different reconstructions. The reconstruction algorithms were used with and without TOF to evaluate the effect of TOF information.

3.2.1 Q-Clear reconstruction

Figure 9 demonstrates CR as a function of BV for the Q-clear reconstruction algorithm with varying β-values from 100 to 1000. The results show that the CR and BV increased when the β-value decreased. With lower β-values the image noise increased. A higher SBR resulted in a higher CR value. The comparison between PET systems that PET images from Discovery MI gave higher CR and lower BV values than Signa. Figure 9 shows higher CR and lower BV with TOF compared to without TOF. Higher BV values were observed in 13, 17, and 22 mm spheres with increased sphere size for PET images on the Signa system. For 22 mm spheres, the Discovery MI showed a small increase in CR with varying β-values. These results are further presented in Appendix.

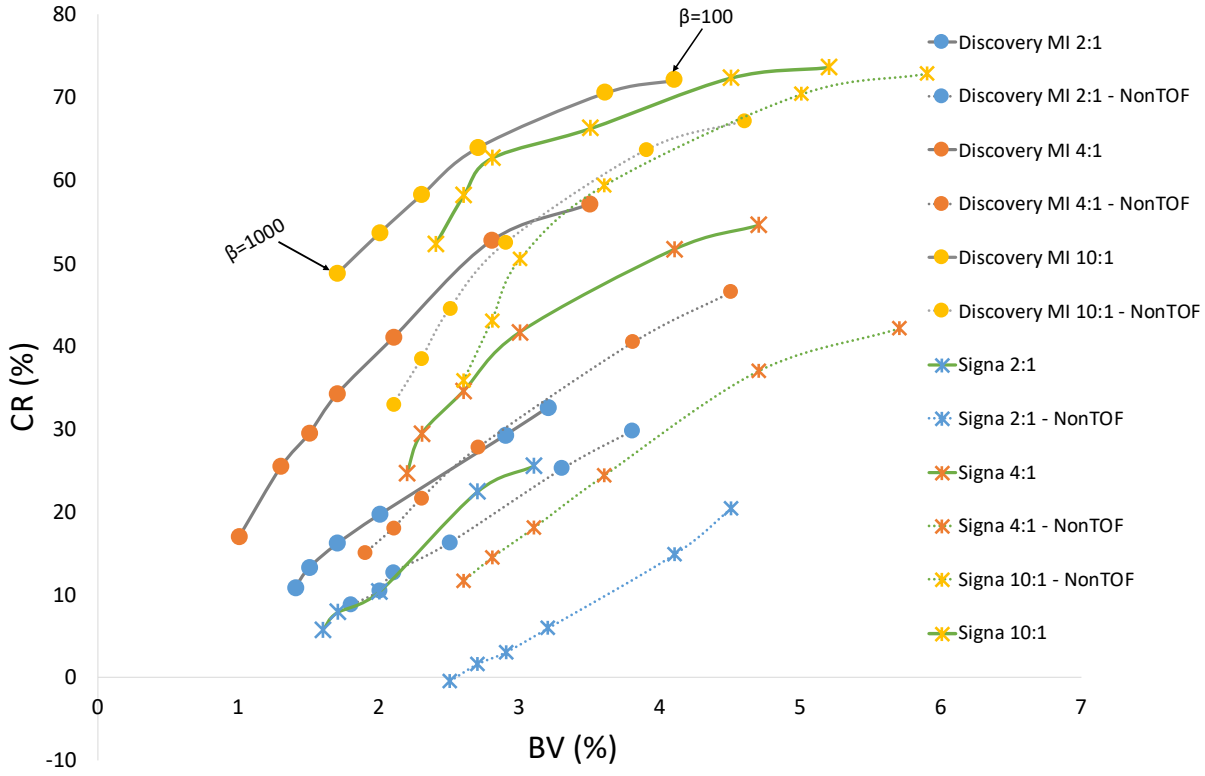

Figure 9: CR versus background variability for the smallest hot sphere (10 mm) with a matrix size of 256x256 and 5 mm FWHM Gaussian filter. Each symbol represents one β-value, starting from β=100 from the right to β=1000. The values from left to right represent a decreased number of β-values (1000-100) of the BPL algorithm. The dashed lines represent data without TOF information, while solid lines represent data with TOF.

For the 10 mm hot sphere, there was a significant difference ($P<0.05$) in CR and BV values obtained by different SBR with different β-values. The ANOVA test illustrated no significant differences in CR and BV values between Signa and Discovery MI systems ($P>0.05$).

A β-value higher than 750 resulted in reduced CR level substantially. The optimum β-value for the 10 mm sphere and 4:1 and 10:1 SBR values was around 150-350 for both Signa and Discovery MI systems. For a lower SBR value, as 2:1, a low β-value gave more accurate CR without increasing the image noise.

3.2.2 OSEM reconstruction

The relation between CR and BV for different number of iterations in OSEM reconstruction is shown in figure 10 for different SBRs. In general, BV increased with an increased number of iterations for all SBR value and camera systems. For SBR 2:1, however, increase was not significant for Discovery MI compared to the Signa and Biographs mCT, and even other SBR values. Biograph mCT showed the highest BV for all activity ratios compared to the other systems, and the same result was obtained for all hot spheres (see figure 16, figure 17, and figure 18 in the Appendix). This high BV can affect the visibility of hot and cold spheres in the reconstructed image. For SBR 10:1, BV increased with the number of iterations, while the CR remained almost constant. The variations of CR and BV with the number of iterations for the non-TOF and TOF reconstructions were similar. The non-TOF reconstruction gave higher BV and lower CR. The results from OSEM reconstruction with non-TOF can be seen in Appendix (figure 15).

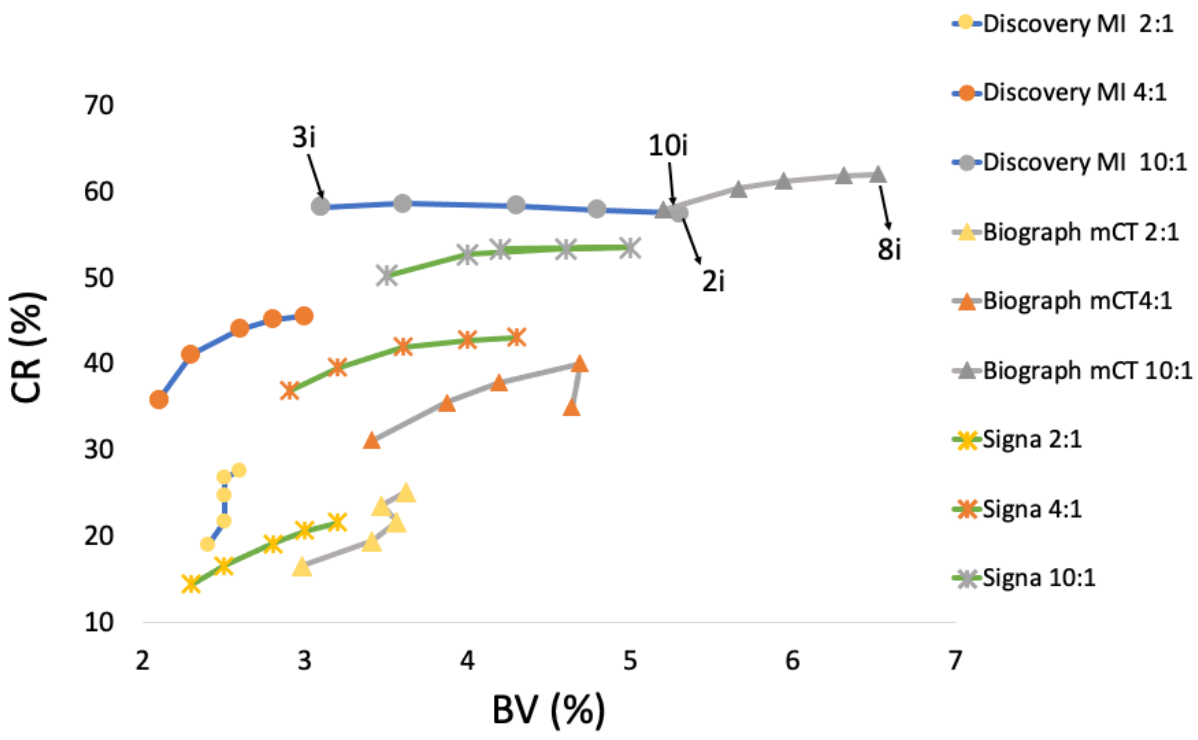

Figure 10: CR plotted against BV for the smallest hot sphere (10 mm). The number of iterations varied (left to right = 3i, 4i, 6i, 8i, 10i for Discovery MI and Signa and 2i,3i,4i,6i,8i for Biograph mCT camera for respective SBR (2:1, 4:1,

10:1). Subsets were kept constant for all reconstructions (16s for Discovery MI and Signa and 21s for Biograph mCT). Matrix sizes of 256x256 and 5 mm FWHM Gaussian filters were kept constant.

ANOVA test showed a statistically significant difference between the systems and SBRs for the 10 mm hot sphere CR ($P<0.05$) and BV ($P<0.05$), with the varied number of iterations.

The optimum number of iterations should reduce image noise without compromising quantification. For imaging ROI with high activity concentrations, reconstruction should be performed with a low number of iterations such as three iterations and 16 subsets for Signa and Discovery MI and two iterations and 21 subsets for Biograph mCT, in order to achieve the best image quality with acceptable BV. Furthermore, SBR 2:1 did not show a large increase of BV with an increased number of iterations. It would be more suitable to use a higher number of iterations to obtain the best contrast in the image as possible in the region of low activity concentration. SBR 4:1 data showed an increase in CR and BV with the number of iterations, so it would be best to find a trade-off between BV and CR by analysing the image, but six iterations can be a good choice.

3.3 Quantitative comparison between OSEM and Q-Clear reconstruction.

Figure 11 illustrates the ratio between CR from Q-clear and CR from OSEM reconstructions for different SBR values. The β-value was 150 for SBR 2:1 and 350 for SBR 4:1 for both cameras. For SBR 10:1, the β-value was 150 for Discovery MI and 350 for Signa. In comparison, the OSEM parameters were three iterations and 16 subsets for all plots.

Figure 11 demonstrates that the ratio reduced with sphere size, and there was less than a 5% difference in value between Signa and Discovery MI cameras for all sphere sizes. The ratio was higher than one for all results, and there was a statistically significant difference in CR between OSEM and the Q-clear algorithms ($P<0.05$). This means that there was always an improvement in image quantification with Q-clear.

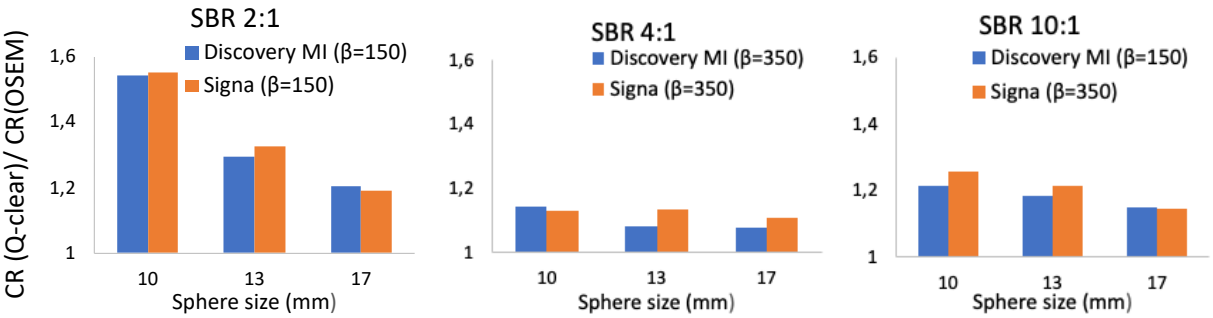

Figure 11: CR(Q-clear)/CR(OSEM) value as a function of sphere size for SBR 2:1, 4:1 and 10:1. β-value was 150 or 350 and OSEM parameters were three iteration and 16 subsets for both cameras. Both reconstructions were made with constant matrix size (256x256) and Gaussian filter (5 mm).

4. Discussion

Multimodality imaging with 2-[^{18}F]FDG in PET/MR and PET/CT systems has opened a new field in clinical oncologic imaging due to its ability to combine functional and structural information using a single device and in a single imaging session. In this study, the PET images from Signa, Discovery MI, and Biograph mCT PET systems were analyzed using the NEMA IQ phantom, which is the standard method to assess the performance of PET systems (44). The PET image quality and quantification accuracy for different SBR levels were investigated by measuring CR and BV in images obtained with different reconstruction algorithms and parameters.

CR results showed the same trend for all SBR values and camera systems: CR decreased with increased β-value (in BPL reconstruction method) and decreased with the increased number of iterations (in OSEM reconstruction method). There was also a general increase in CR with increased sphere size. The size of the sphere is in practice difficult to derive from PET images due to the partial volume effect. Ideally, CR should be 100% for the ROI, but the partial volume effect in PET images can result in an overestimation or underestimation (or loss) of activity in the ROI due to spill-in and spill-out effects (45).

CR was higher for the GE PET/CT camera compared with the GE PET/MRI system. BV decreased with increased β-value for both cameras, where BV reflects the noise level of the image. In

OSEM reconstruction, CR reached a plateau for SBR 10:1 with increased number of iterations, while BV increased.

The results present that Q-clear with TOF using a β-value between 150 and 350 for GE PET/MRI and GE PET/CT is an appropriate choice to use for Q-clear reconstruction. β-values were chosen as a trade-off between contrast improvement and remaining at the same noise level as OSEM. The optimal OSEM was with TOF information using three iterations, 16 subsets, and 5 mm FWHM Gaussian filter for GE Discovery MI and GE Signa systems, and two iterations, 21 subsets, and 5 mm FWHM Gaussian filter for Siemens Biograph mCT system.

The optimal reconstruction algorithms and parameters cannot be directly applied for clinical imaging because the present study is based on a simplified situation using the NEMA phantom. Further studies are needed to examine how clinical PET images should be analysed, including choice of reconstruction algorithm, parameters, depending on the T/B ratio

A previous study based on a NEMA phantom experiment has compared Q-clear reconstruction parameters with OSEM reconstruction with three iterations, 16 subsets, and a Gaussian post-filter with FWHM of 5.0 mm (46). The results of that study suggested that the optimal β-value depends on the contrast and the lesion's size. A high β-value can lead to a negative impact on the detectability of the small lesion. It was then suggested that β-values ranging between 300 and 400 will maximise the CR and contrast-to-noise ratio (CNR) for small spheres. This β-value range from that study is similar as the results from the present study, where we found the best trade-off between CR and BV was achieved with a β-value of 350 for SBR 10:1 and SBR 4:1. Another study evaluated and compared PET image reconstruction algorithms on image quality and quantitative parameters in patients with initial lung cancer using a PET/CT scanner (47). Those results showed an increased image quality, image sharpness, and tumor lesion conspicuity with Q-clear compared to OSEM. It was even suggested to adjust β-values to the injected 2-[^{18}F]FDG activity to provide more patient-tailored PET imaging and for maintaining image quality, while reducing the absorbed dose to the patient. A lower dose is especially highly

preferred for young patients. A higher β-value (450 - 600) was suggested to be more appropriate for a patient, who received lower 2-[^{18}F]FDG activity (< 2 MBq/kg) compared with patients who received higher activity (> 2 MBq/kg).

Previous studies have compared 2-[^{18}F]FDG PET images from whole-body PET/CT (Siemens Biograph and GE Discovery VCT) with integrated PET/MRI (Siemens Biograph mMR) systems in detection and anatomic localisation of lesions. Although the scanners have different PET detector technologies, the results showed an agreement rate of 97%-98% in 32-80 patients with various malignant lesions (48, 49). In another study, a somewhat lower agreement was obtained, i.e., 94%, probably due to the choice of MRI protocol, the acquisition time of PET, and time for scan after injection (50). These factors may also have influenced the results of the present study (except for the MRI protocol, which was not used for PET/MRI scans). For example, a short acquisition time results in increased noise level and decreased contrast in the acquired PET images. There are other factors that can impact the spatial resolution in PET imaging. The factors are the difference in PET acquisition technologies between systems, such as the type of detector and the size of detector crystal, crystal penetration, partial volume effect and sampling error (51). According to the present results and the hardware differences between systems, the Signa and Discovery MI systems gave overall better performance than Biograph mCT in our study, most notably for the BV result.

The difference in system technology and reconstruction methods can affect image quality and the quantification of CR for phantom or the SUV for oncological imaging (48). This effect has been shown in two earlier studies that have reported discrepancies in lesion-to-background SUV measured in the PET/MRI and PET/CT systems. One of the studies observed significantly lower SUVs for PET data acquired with PET/MRI than PET/CT for the assessed lesions and different organ systems (48). In contrast, the other study observed the opposite, where the differences between the systems could even depend on the various time intervals between the two scans. The lesion SUV is in general expected to increase over time (49) due to higher activity concentration differences between tumor and normal tissues (52).

The clinical performance of PET/MRI compared with PET/CT has also been evaluated in mixed cancer patient populations (49, 50, 53, 54). As excepted, PET/CT detected more lesions overall, especially in the lungs. This is due to MRI having lower detectability of small lung lesions, the large thickness of MRI images, and the difference in the performance of the PET scanners. In contrast, PET/MRI had higher diagnostic accuracy performance (+ 13%) than PET/CT for detecting brain and liver metastases due to superior soft-tissue contrast in MRI. Therefore, one of the studies summarised that PET/CT is more likely to be the preferred imaging system for lung and mediastinal nodal disease (49).

The present study had several limitations due to limited scan time possibilities on the clinical system. One of them is that only one scan per activity concentration was performed for each system. More than two scans had been needed to get a more accurate statistical analysis (55). Another limitation was that for some scans the PET acquisition time had to be reduced from the originally planned time schedule, based on the availability of each system.

Another possible parameter to analyze is CNR for better harmonization of this study result. Then, the detectability between the systems for different reconstruction algorithms and parameters could have been compared. CNR gives information about the visibility of a lesion, while CR gives information on how accurately the system can measure the activity concentration in the lesion. In future studies on clinical images, CNR should also be evaluated.

This study had a source of error in phantom preparation because the NEMA phantom was filled with a volumetric flask, which affected the accuracy and precision of radioactivity concentrations in hot spheres and phantom backgrounds. A lab-scaler with more significant digits should be used for more accurate measurement. Furthermore, the ROIs were drawn automatically based on the software of the workstations, which reduced the random uncertainty that can occur by manually positioning. Nevertheless, there might be a systematic

error due to the difference between softwares used in the Siemens Biograph mCT and GE-Signa and Discovery MI systems workstations.

5. Conclusion

The reconstruction algorithm comparison showed that Q-clear gave higher CR and lower BV values with Q-clear than with OSEM. Sphere with higher SBR values gave a higher noise level with increased number of iterations. While those with lower SBR values gave increased contrast levels with the increased number of iterations. High β-value gave a lower noise level and poorer contrast. Thus, the Q-Clear resulted in better PET image quality and quantitative assessment than OSEM.

Comparing the performance of the systems to detect the smallest sphere (10 mm) with the Q-clear algorithm, showed a higher CR and lower BV for PET images from GE Discovery MI than GE Signa systems. The Siemens Biograph mCT, which only uses the OSEM algorithm, gave the lowest performance due to higher BV, which indicates a higher noise level in the image.

6. Acknowledgment

I would like to thank my supervisors Esmaeil Mehrara, Eva Forssell-Aronsson, and Tobias Rosholm for all their support, guidance, and presence through this project. A special thanks to Esmaeil and Tobias for being tremendously supportive and patient throughout all long scanning days. I would also like to thank my family, husband, and friends for all the positive encouragement.

Reference list

1. Tubiana M. [Wilhelm Conrad Rontgen and the discovery of X-rays]. Bull Acad Natl Med. 1996;180(1):97-108.
2. Morris P PA. Diagnostic imaging. Lancet. 2012 Apr 21.
3. Jones T, Townsend D. History and future technical innovation in positron emission tomography. J Med Imaging (Bellingham). 2017;4(1):011013.
4. Ashraf MA, Goyal A. Fludeoxyglucose (18F). StatPearls. Treasure Island (FL)2021.
5. Almuhaideb A, Papathanasiou N, Bomanji J. 18F-FDG PET/CT imaging in oncology. Ann Saudi Med. 2011;31(1):3-13.
6. Kim N, Cho H, Yun M, Park KR, Lee CG. Prognostic values of mid-radiotherapy (18)F-FDG PET/CT in patients with esophageal cancer. Radiat Oncol. 2019;14(1):27.
7. Cherry SR, Sorenson JA, Phelps ME. Physics in nuclear medicine. 4th ed. Philadelphia: Elsevier/Saunders; 2012. 25, 307 p.
8. Bailey DL. Positron emission tomography : basic sciences. New York: Springer; 2005. 64, 92. p.
9. Turkington TG. Introduction to PET instrumentation. J Nucl Med Technol. 2001;29(1):4-11.
10. Vandenberghe S, Moskal P, Karp JS. State of the art in total body PET. EJNMMI Phys. 2020;7(1):35.
11. Fahey FH. Data acquisition in PET imaging. J Nucl Med Technol. 2002;30(2):39-49.
12. Cherry SR, Sorenson JA, Phelps ME. Physics in nuclear medicine. 4th ed. Philadelphia: Elsevier/Saunders; 2012. 330, 40 p.
13. Valk PE. Positron emission tomography : basic science and clinical practice. London ; New York: Springer; 2003. 92-3 p.
14. Tong S, Alessio AM, Kinahan PE. Image reconstruction for PET/CT scanners: past achievements and future challenges. Imaging Med. 2010;2(5):529-45.
15. Valk PE. Positron emission tomography : basic science and clinical practice. London ; New York: Springer; 2003. 201-3 p.

16. Carney JPJ, Townsend DW, Rappoport V, Bendriem B. Method for transforming CT images for attenuation correction in PET/CT imaging. Med Phys. 2006;33(4):976-83.
17. Cherry SR, Sorenson JA, Phelps ME. Physics in nuclear medicine. 4th ed. Philadelphia: Elsevier/Saunders; 2012. 358 p.
18. Alameen S, Tamam N, Awadain S, Sulieman A, Alkhaldi L, Hmed AB. Radiobiological risks in terms of effective dose and organ dose from (18)F-FDG whole-body PET/CT procedures. Saudi J Biol Sci. 2021;28(10):5947-51.
19. Icrp. Radiation dose to patients from radiopharmaceuticals. Addendum 3 to ICRP Publication 53. ICRP Publication 106. Approved by the Commission in October 2007. Ann ICRP. 2008;38(1-2):1-197.
20. Kaushik A, Jaimini A, Tripathi M, D'Souza M, Sharma R, Mondal A, et al. Estimation of radiation dose to patients from (18) FDG whole body PET/CT investigations using dynamic PET scan protocol. Indian J Med Res. 2015;142(6):721-31.
21. Cherry SR, Sorenson JA, Phelps ME. Physics in nuclear medicine. 4th ed. Philadelphia: Elsevier/Saunders; 2012. 360-1 p.
22. Grant AM, Deller TW, Khalighi MM, Maramraju SH, Delso G, Levin CS. NEMA NU 2-2012 performance studies for the SiPM-based ToF-PET component of the GE SIGNA PET/MR system. Med Phys. 2016;43(5):2334.
23. Caribe P, Vandenberghe S, Diogo A, Perez-Benito D, Efthimiou N, Thyssen C, et al. Monte Carlo Simulations of the GE Signa PET/MR for Different Radioisotopes. Front Physiol. 2020;11:525575.
24. Wagenknecht G, Kaiser HJ, Mottaghy FM, Herzog H. MRI for attenuation correction in PET: methods and challenges. MAGMA. 2013;26(1):99-113.
25. Chen Y, An H. Attenuation Correction of PET/MR Imaging. Magn Reson Imaging Clin N Am. 2017;25(2):245-55.
26. Ziegler S, Jakoby BW, Braun H, Paulus DH, Quick HH. NEMA image quality phantom measurements and attenuation correction in integrated PET/MR hybrid imaging. Ejnmmi Phys. 2015;2(1).

27. Kurita Y, Ichikawa Y, Nakanishi T, Tomita Y, Hasegawa D, Murashima S, et al. The value of Bayesian penalized likelihood reconstruction for improving lesion conspicuity of malignant lung tumors on F-18-FDG PET/CT: comparison with ordered subset expectation maximization reconstruction incorporating time-of-flight model and point spread function correction. Ann Nucl Med. 2020;34(4):272-9.

28. Tsutsui Y, Awamoto S, Himuro K, Umezu Y, Baba S, Sasaki M. Edge Artifacts in Point Spread Function-based PET Reconstruction in Relation to Object Size and Reconstruction Parameters. Asia Ocean J Nucl Med Biol. 2017;5(2):134-43.

29. Teoh EJ, McGowan DR, Macpherson RE, Bradley KM, Gleeson FV. Phantom and Clinical Evaluation of the Bayesian Penalized Likelihood Reconstruction Algorithm Q.Clear on an LYSO PET/CT System. J Nucl Med. 2015;56(9):1447-52.

30. Otani T, Hosono M, Kanagaki M, Onishi Y, Matsubara N, Kawabata K, et al. Evaluation and Optimization of a New PET Reconstruction Algorithm, Bayesian Penalized Likelihood Reconstruction, for Lung Cancer Assessment According to Lesion Size. AJR Am J Roentgenol. 2019;213(2):W50-W6.

31. Vallot D, Caselles O, Chaltiel L, Fernandez A, Gabiache E, Dierickx L, et al. A clinical evaluation of the impact of the Bayesian penalized likelihood reconstruction algorithm on PET FDG metrics. Nucl Med Commun. 2017;38(11):979-84.

32. te Riet J, Rijnsdorp S, Roef MJ, Arends AJ. Evaluation of a Bayesian penalized likelihood reconstruction algorithm for low-count clinical F-18-FDG PET/CT. Ejnmmi Phys. 2019;6(1).

33. Ziegler S, Jakoby BW, Braun H, Paulus DH, Quick HH. NEMA image quality phantom measurements and attenuation correction in integrated PET/MR hybrid imaging. EJNMMI Phys. 2015;2(1):18.

34. Association. NEM. “NEMA Standards Publication NU 2–2007, Performancemeasurements of positron emission tomographs”. Rosslyn, VA. 2007:26–33.

35. Cherry SR, Phelps ME, Sorenson JA. Physics in Nuclear Medicine: W B Saunders Company; 2012.

36. Cherry SR, Sorenson JA, Phelps ME. Physics in nuclear medicine. 4th ed. Philadelphia: Elsevier/Saunders; 2012. 299-300 p.

37. Kosaka N, Tsuchida T, Uematsu H, Kimura H, Okazawa H, Itoh H. 18F-FDG PET of common enhancing malignant brain tumors. AJR Am J Roentgenol. 2008;190(6):W365-9.

38. Liu Y. Focal mass-like cardiac uptake on oncologic FDG PET/CT: Real lesion or atypical pattern of physiologic uptake? J Nucl Cardiol. 2019;26(4):1205-11.

39. Rijnsdorp S, Roef MJ, Arends AJ. Impact of the Noise Penalty Factor on Quantification in Bayesian Penalized Likelihood (Q.Clear) Reconstructions of (68)Ga-PSMA PET/CT Scans. Diagnostics (Basel). 2021;11(5).

40. Straver ME, Aukema TS, Olmos RA, Rutgers EJ, Gilhuijs KG, Schot ME, et al. Feasibility of FDG PET/CT to monitor the response of axillary lymph node metastases to neoadjuvant chemotherapy in breast cancer patients. Eur J Nucl Med Mol Imaging. 2010;37(6):1069-76.

41. SIGNA™ PET/MR Technical Data. GE Healthcare.

42. Discovery MI with LightBurst Digital 4-Ring Detector. GE Healthcare 2016.

43. Siemens Biograph mCT Technical Specifications.

. 15 dec 2021:https://www.siemens-healthineers.com/en-us/molecular-imaging/pet-ct/biograph-mct.

44. DiscoveryTM MI and DiscoveryTM MI Columbia User Manual, Revision 6. 2019:Revision 6.

45. National Electrical Manufacturers Association. NEMA Standards Publication NU 2–2007 Pmo, tomographs: pe. https://www.nema.org. 2007, Accessed 14 Dec 2018: p. 26–33.

46. Caribe P, Koole M, D'Asseler Y, Van Den Broeck B, Vandenberghe S. Noise reduction using a Bayesian penalized-likelihood reconstruction algorithm on a time-of-flight PET-CT scanner. EJNMMI Phys. 2019;6(1):22.

47. Messerli M, Stolzmann P, Egger-Sigg M, Trinckauf J, D'Aguanno S, Burger IA, et al. Impact of a Bayesian penalized likelihood reconstruction algorithm on image quality in novel digital PET/CT: clinical implications for the assessment of lung tumors. EJNMMI Phys. 2018;5(1):27.

48. Drzezga A, Souvatzoglou M, Eiber M, Beer AJ, Furst S, Martinez-Moller A, et al. First clinical experience with integrated whole-body PET/MR: comparison to PET/CT in patients with oncologic diagnoses. J Nucl Med. 2012;53(6):845-55.

49. Al-Nabhani KZ, Syed R, Michopoulou S, Alkalbani J, Afaq A, Panagiotidis E, et al. Qualitative and quantitative comparison of PET/CT and PET/MR imaging in clinical practice. J Nucl Med. 2014;55(1):88-94.

50. Ishii S, Shimao D, Hara T, Miyajima M, Kikuchi K, Takawa M, et al. Comparison of integrated whole-body PET/MR and PET/CT: Is PET/MR alternative to PET/CT in routine clinical oncology? Ann Nucl Med. 2016;30(3):225-33.

51. Oen SK, Aasheim LB, Eikenes L, Karlberg AM. Image quality and detectability in Siemens Biograph PET/MRI and PET/CT systems-a phantom study. EJNMMI Phys. 2019;6(1):16.

52. Baun C, Falch K, Gerke O, Hansen J, Nguyen T, Alavi A, et al. Quantification of FDG-PET/CT with delayed imaging in patients with newly diagnosed recurrent breast cancer. BMC Med Imaging. 2018;18(1):11.

53. Mayerhoefer ME, Prosch H, Beer L, Tamandl D, Beyer T, Hoeller C, et al. PET/MRI versus PET/CT in oncology: a prospective single-center study of 330 examinations focusing on implications for patient management and cost considerations. Eur J Nucl Med Mol Imaging. 2020;47(1):51-60.

54. Lee SM, Goo JM, Park CM, Yoon SH, Paeng JC, Cheon GJ, et al. Preoperative staging of non-small cell lung cancer: prospective comparison of PET/MR and PET/CT. Eur Radiol. 2016;26(11):3850-7.

55. Cherry SR, Sorenson JA, Phelps ME, ScienceDirect. Physics in nuclear medicine. 4th ed. Philadelphia: Elsevier/Saunders; 2012. 136-40 p.

Appendix

The figure below shows the CR versus BV for 13, 17 and 22 mm hot spheres, reconstructed with Q-clear reconstruction algorithm.

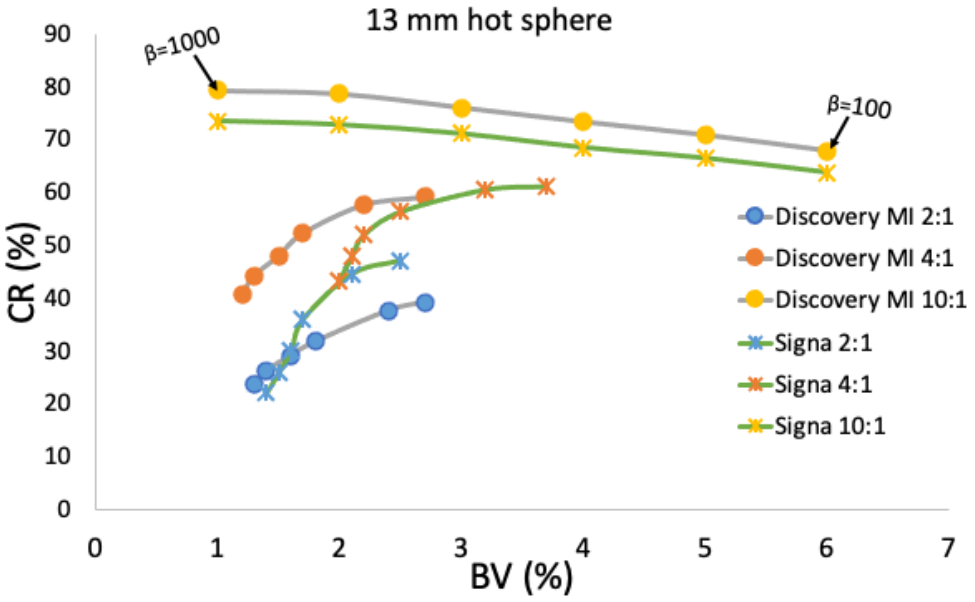

Figure 12: CR versus BV for the 13 mm hot sphere reconstructed with Q-clear + TOF. Each symbol represents one β-value, starting from β 100 from the right to β 1000. Matrix size of 256x256 and 5 mm FWHM Gaussian filter were kept constant for all reconstruction.

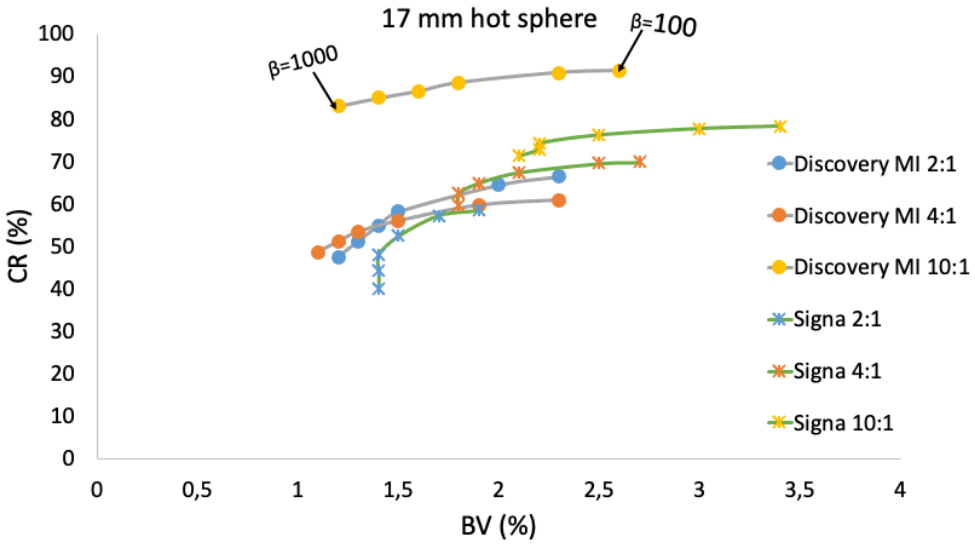

Figure 13: CR versus BV for the 17 mm hot sphere reconstructed with Q-clear + TOF. Each symbol represents one β-value, starting from β=100 from the right to β=1000. Matrix size of 256x256 and 5 mm FWHM Gaussian filter were kept constant for all reconstruction.

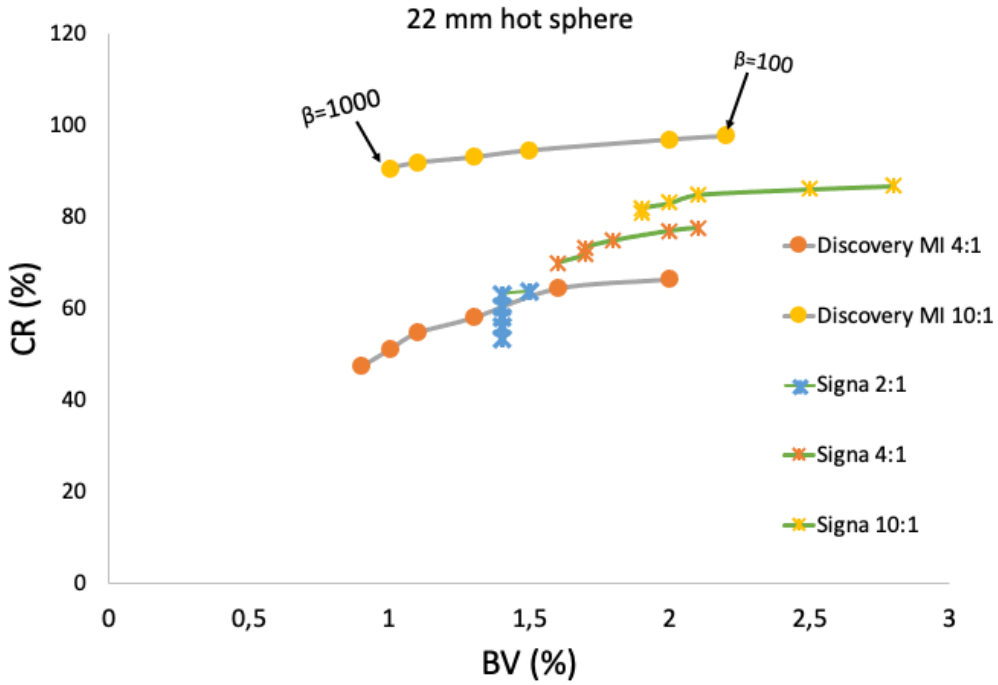

Figure 14: CR versus BV for the 17 mm hot sphere reconstructed with Q-clear + TOF. Each symbol represents one β-value, starting from β 100 from the right to β 1000. Matrix size of 256x256 and 5 mm FWHM Gaussian filter were kept constant for all reconstruction.

The result of OSEM reconstruction without TOF (NonTOF) for varying number of iterations.

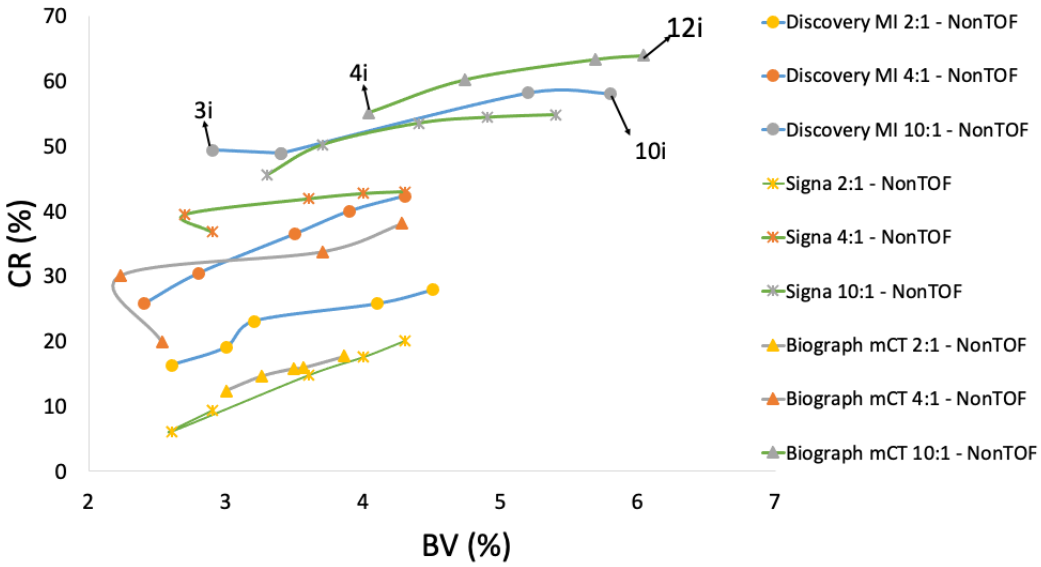

Figure 15: CR versus BV for varying iteration without TOF (left to right = 3i, 4i, 6i, 8i, 10i for Discovery MI and Signa and 4i,6i,8i,10i,12i for Biograph camera). All reconstructions had constant subset (16s for Discovery MI and Signa and 12s for Biograph mCT), matrix size of 256x256, and 5 mm FWHM Gaussian.

The results below represent BV against CR for 13, 17 and 22 mm hot spheres, reconstructed with OSEM+TOF.

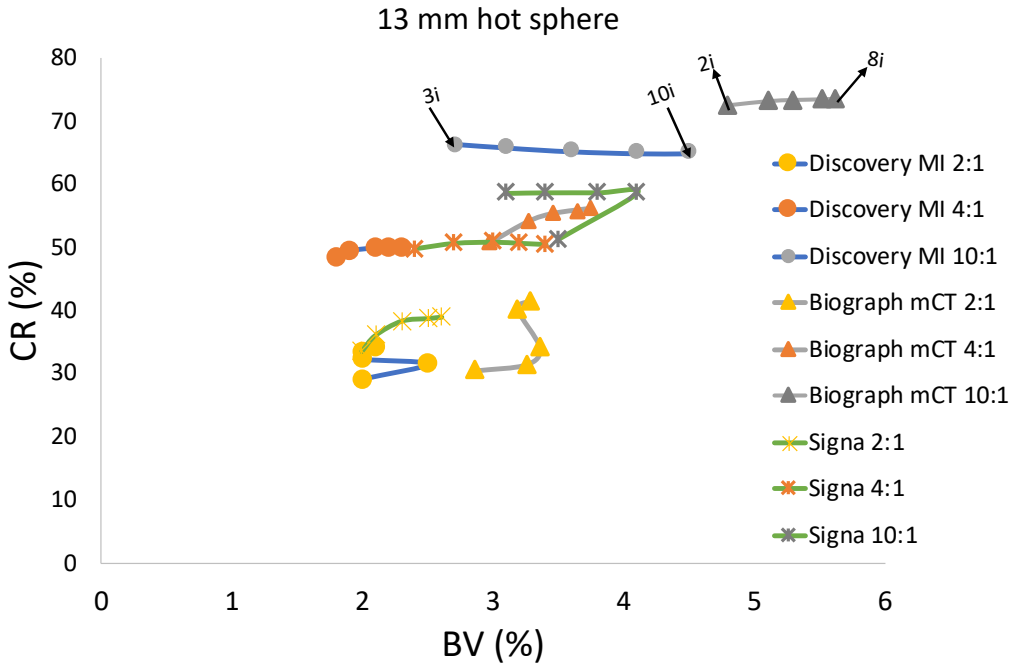

Figure 16: CR as a function of BV for 13 mm hot sphere, there iterations varied (left to right = 3i, 4i, 6i, 8i, 10i for Discovery MI and Signa and 2i,3i,4i,6i,8i for Biograph mCT). Subsets were kept constants for all reconstructions (16s for Discovery MI and Signa and 21s for Biograph mCT). Matrix size of 256x256 and 5 mm FWHM Gaussian filter were kept constant.

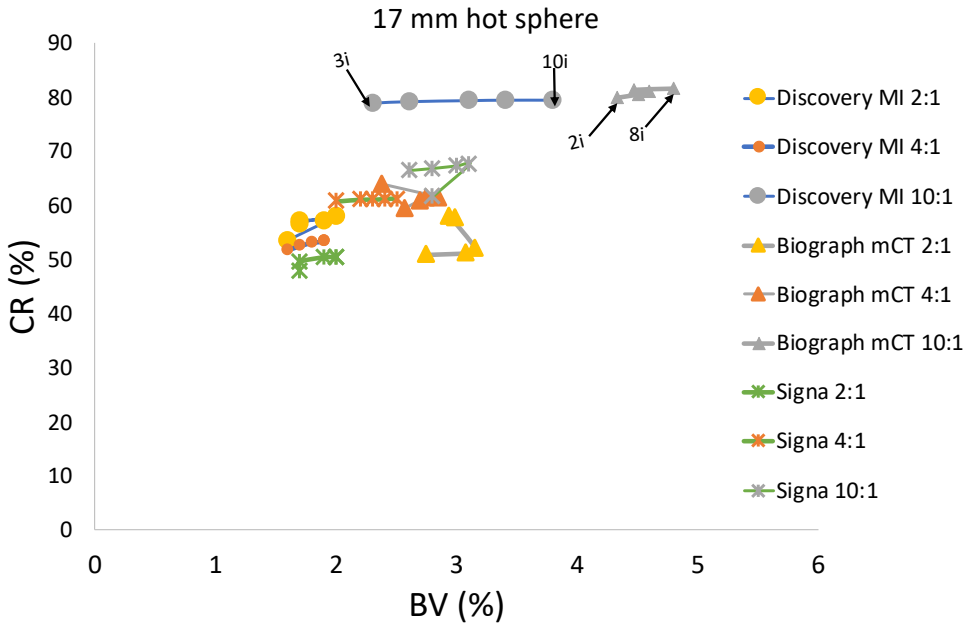

Figure 17: CR versus BV for 17 mm hot sphere, with varying iterations (left to right = 3i, 4i, 6i, 8i, 10i for Discovery MI and Signa and 2i,3i,4i,6i,8i for Biograph mCT camera). Subsets were kept constants for all reconstructions (16s for Discovery MI and Signa and 21s for Biograph mCT). Matrix size of 256x256 and 5 mm FWHM Gaussian filter were also kept constant.

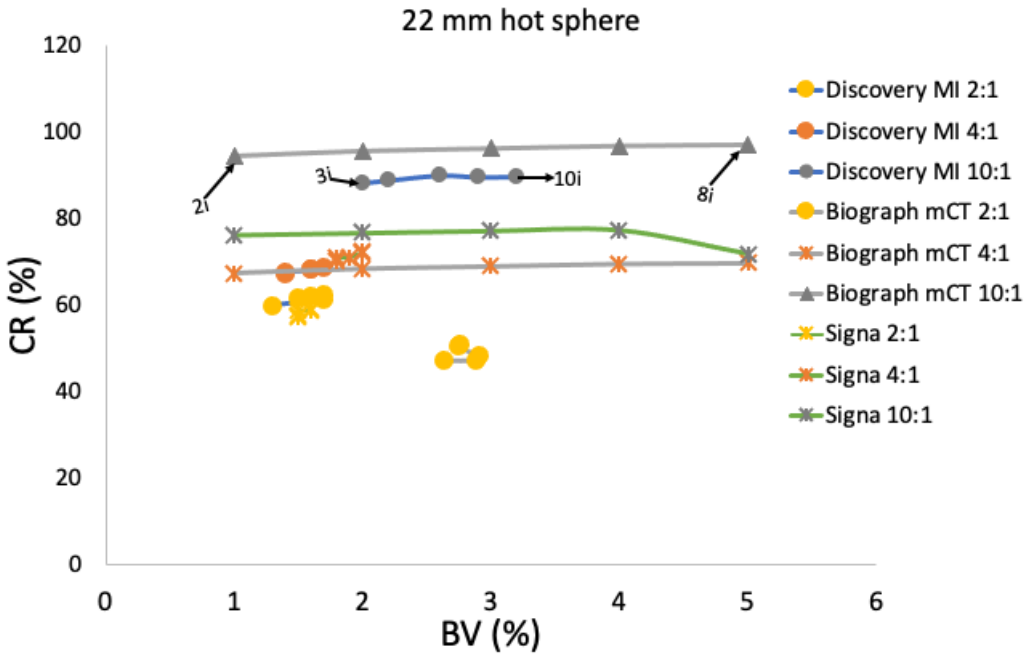

Figure 18: CR versus BV for 22 mm hot sphere, with varying iterations (left to right = 3i, 4i, 6i, 8i, 10i for Discovery MI and Signa and 2i,3i,4i,6i,8i for Biograph mCT). Subsets were kept constants for all reconstructions (16s for Discovery MI and Signa and 21s for Biograph mCT). Matrix size of 256x256 and 5 mm FWHM Gaussian filter were also kept constant.